Energy & Environmental Science

Accepted Manuscript

ROYAL SOCIETY OF CHEMISTRY

www.rsc.org/ees

Journal Name

ARTICLE

A high-rate and long cycle life solid-state lithium-air battery

X. B. Zhu, T. S. Zhao,* Z. H. Wei, P. Tan and L. An

Received 00th January 20xx,
Accepted 00th January 20xx

DOI: 10.1039/x0xx00000x

www.rsc.org/

Lithium-air batteries are currently limited to being operated under pure oxygen rather than ambient air, primarily due to the discharge product, lithium peroxide, reacting with water and carbon dioxide in ambient air to produce lithium carbonate, which renders the battery irreversible. A solution to this debilitating problem is to install an oxygen selective membrane that only allows oxygen to enter the battery. While theoretically sound, this method causes a significant decrease in the oxygen transfer rate due to a limited oxygen permeation area of the planar membrane and an increase in the oxygen transport distance from the membrane to the reaction sites. In this work, we create a novel solid-state lithium-air battery having a porous LATP cathode, designed with silicone-oil films coated pores that block water vapor and carbon dioxide from reaching reaction sites, but allow a high rate of oxygen transfer owing to an increase in the specific area of the films and a reduced oxygen transfer resistance. This battery can operate with ambient air at 5,000 mA h g^{-1}_{carbon} for 50 cycles (125 days). Moreover, the charge/discharge rate reaches as high as 2.0 mA cm^{-2}, a value which is about 40 times higher than that of conventional lithium-air batteries having an oxygen selective membrane external to the cathode.

Introduction

The world's energy demands have been steadily increasing over the years, with an ever widening gap between demand and supply, particularly in emerging industries such as electric vehicles.[1-4] The need to switch from fossil-fueled transportation to electric cars will be an undoubtable movement in the near future, helping to relieve climate change and securing energy sustainability. Development in this area, however, has slowed down considerably due to a lack of satisfactory electrical energy-storage systems.[5,6] A promising candidate is the lithium-air battery, possessing advantages of being a portable power source and exhibiting the highest theoretical specific energy density of 11,680 W h kg^{-1}_{Li} among known metal-based electrochemical batteries.[7-9] Its high energy density owes to two major reasons: (i) lithium, as the lightest metal, possesses a high specific capacity of 3,860 mA h g^{-1}; and (ii) oxygen, as one of the reactants, can theoretically be obtained from ambient air without occupying the battery's volume and mass. Its energy density is so enticing that can be comparable to that of gasoline (13,000 W h kg^{-1}), which means that it meets the necessary demands required to power an electric vehicle.[10,11] Consequently, interest in this area has increased considerably in recent years.[12-15]

Although promising, several issues exist in practical lithium-air battery operation and must be resolved before widespread commercialization is possible. One major issue is associated with the use of liquid electrolytes, which causes several problems including leakage, evaporation, flammability (as organic contents), low oxygen solubility/diffusion (usually considered as the rate-limiting step) and chemical and/or electrochemical instabilities (organic liquid electrolytes are generally unstable and easily decomposed by the superoxide anion radical *via* nucleophilic attack).[2,16-20] To address these problems, a solid-state lithium-air battery system has been developed with the introduction of solid-state Li-ion conductors.[12,21] The electrolyte is stable and has a satisfactory Li^+ conductivity.[10,22] In addition, the solid-state electrolyte layer can act as a barrier to protect the Li anode from moisture, oxygen, carbon dioxide and nitrogen in the air, significantly improving the stability of lithium-air batteries for long-term operation. Moreover, the solid-state electrolyte can serve as a physical barrier to avoid short circuiting caused by Li dendrites during operation.[10,23] Another major issue comes from the lithium-air battery's unique open system feature.[24-27] This invites impurities, such as, H_2O and CO_2 in ambient air to react with the discharge product Li_2O_2, forming undesirable side products (*e.g.*, LiOH and Li_2CO_3), which have been reported to be difficult to remove even at high charge voltages, resulting in a low energy efficiency and short cycle life.[28,29] To circumvent this problem, most reports have suggested that lithium-air batteries are to be operated in pure oxygen instead of ambient air.[30,31] One strategy is to introduce an oxygen selective membrane (OSM) that only allows oxygen into the cathode, which blocks undesirable components, especially moisture.[32,33]

Zhang et al. developed an oxygen-selective immobilized liquid membrane for direct operation of non-aqueous lithium-air battery in ambient air (20-30% relative humidity).[34] The membrane was prepared by soaking high viscosity silicone oil into porous metal or Teflon substrates. The selectivity (O_2 to H_2O) of the membrane reached 3.6 due to a higher solubility

Department of Mechanical and Aerospace Engineering, The Hong Kong University of Science and Technology, Clear Water Bay, Kowloon, Hong Kong SAR, China. E-mail: metzhao@ust.hk (T.S. Zhao)

and/or diffusivity of O_2 than that of H_2O in silicone oil. A lithium-air battery with this OSM can be operated in ambient air for 16.3 days at a constant current density of 0.05 mA cm^{-2} achieving a specific capacity of 789 mA h g^{-1}_{carbon}. The group also developed a dense-phase poly(tetrafluoroethylene) (PTFE) OSM, which enabled a lithium-air battery to operate in ambient air for 21 days with a specific capacity of 1,022 mA h g^{-1}_{carbon} at 0.05 mA cm^{-2}.[35] A heat-sealable polymer membrane was developed by another Zhang's group and used as both an oxygen-diffusion film and a moisture barrier, which enabled a lithium-air battery to operate in ambient air for more than one month with a specific capacity of 362 W h kg^{-1} at 0.05 mA cm^{-2}, based on the total weight of the battery configuration.[36] Crowther et al. used silicone rubbers as OSMs for optimizing the performances of a primary lithium-air battery.[37] The hydrophobic silicone rubber films were coated directly onto the surface of the air electrodes. When discharged in air at 0.2 mA cm^{-2}, the lithium-air battery delivered a specific capacity of 570 mA h g^{-1}.

The integration of solid-state electrolytes with OSMs seems to provide a plausible solution to solve existing problems for the operation of lithium-air batteries in ambient air. However, it will create at least three new technical challenges: (i) High internal resistance for solid-state electrolytes. In conventional solid-state lithium-air batteries, solid-state electrolytes exist independently, demanding a need to set its thickness (150 ~ 800 μm) to meet the required mechanical properties for practical applications. Additionally, Li^+ conductivities for existing solid-state electrolyte materials are reported to be at only a tenth to a hundredth of that for liquid electrolytes, suggesting that the electrolyte layer causes severe ohmic loss; (ii) Limited interface between the solid-state electrolyte and cathode. In conventional solid-state lithium-air batteries, triple-phase boundaries (TPBs) are typically limited to the interfaces between the solid-state electrolyte and cathode, which are much smaller in area than that of lithium-air batteries using liquid electrolytes where cathodes are completely saturated. (iii) Low oxygen selectivity and flux for existing OSMs. OSM types can be classified into two categories, porous and nonporous membranes. Approaches using porous OSMs were largely unsuccessful due to O_2/H_2O selectivity being virtually negligible, but for nonporous OSMs that exhibit adequate oxygen selectivity, the permeation rate is very low.[33,38] Hence, we propose and prepare a novel solid-state lithium-air battery that is composed of three key components: i) an ultra-thin solid-state electrolyte layer (19 μm thick), ii) a porous lithium aluminum titanium phosphate (LATP) cathode, onto whose pore surfaces carbon nanoparticles are deposited for electron conduction, and iii) silicone-oil films (about 50 nm thick), which are coated onto the pore surfaces of the cathode to block water vapor and carbon dioxide from reaching reaction sites. Our results provide evidence of enhanced performance in the discharge capacity, rate capability and cycle life of this solid-state lithium-air battery when actually operating in ambient air.

Experimental

Integrated structure preparation

Supporting information gives the details of this part. $Li_{1.3}Al_{0.3}Ti_{1.7}(PO_4)_3$ (LATP) raw powders with a wide range of particle sizes were prepared *via* two different methods, namely solid-phase reaction and sol-gel.[12,39,40] Sol-gel derived LATP powders were thoroughly mixed with starch at a weight ratio of 6 : 5 and uniaxially pressed into pellets under 200 MPa prior to sintering at 850 °C. The LATP membrane (19 μm thick) was then coated onto one surface of pre-sintered LATP pellets by a slurry spin-coating technique and finally sintered at 1,000 °C to form an integrated structure with a 75% porous cathode-support and a 96% dense electrolyte membrane, as shown in Fig. 1. The ionic conductivity of the porous cathode was measured to be 7.1×10^{-5} S cm^{-1} by a three-electrode method (see Fig. S1). We have also measured the conductivity using the two-electrode set up, and got the same results.

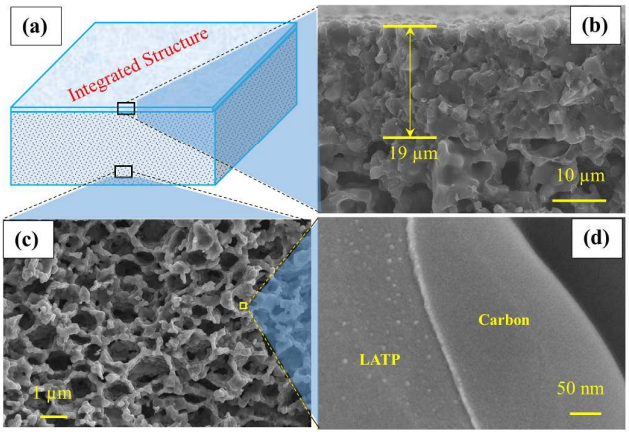

Fig. 1 (a) Schematic illustration for the proposed integrated structure with a dense LATP membrane and a porous LATP cathode-support. The SEM images for (b) a dense LATP membrane seamlessly connected with (c) a porous LATP cathode-support, and (d) carbon nano-particles coated LATP cathode.

Carbon nano-particles coated LATP cathodes preparation

Carbon nano-particles coated LATP cathode was prepared by infiltrating 10 wt% sucrose solution into 75% porous LATP cathode-support. After firing at 650 °C for 3 h in pure Ar, a uniform and thin carbon coating with a loading of 1.8 mg cm^{-2} (projected area) was achieved.

Loading of silicone-oil films into the carbon-coated LATP cathodes

To deposit a silicone-oil film, the carbon-coated LATP cathode was first baked at 200 °C for 20 min. in order to remove the adsorbed water and enhance the wettability of the carbon surface. The silicone oil ($(-Si(CH_3)_2O)n$, Sigma-Aldrich, Co., USA) was prepared into the porous cathode *via* an infiltration process while strictly controlling the volume using a micro-syringe. The cathode was subsequently moved into a vacuum oven and dried at 50 °C for 48 h.

Permeability measurement

The gas permeability of silicone oil was measured using a home-made gas permeation device consisting of a silicone-oil impregnated 95% porous nickel foam in a flow channel (see Fig. S2). A bubble flow meter was used to measure the amount of the permeated gas (mol), F, while a pressure gauge was used to determine the pressure drop across the nickel foam, P_2-P_1 (Pa). The gas permeation rate, M, was determined by

$$M = F \times L \times S^{-1} \times t^{-1} \times (P_2 - P_1)^{-1} \quad (1)$$

where S is the sample surface area (m^2), L is the sample thickness (m), and t is the testing time (h). The permeation rates of O_2 and CO_2 were 6.2 ~ 9.4 × 10^{-7} mol m^{-1} h^{-1} Pa^{-1} and 4.7 ~ 6.3 × 10^{-7} mol m^{-1} h^{-1} Pa^{-1}, respectively. In addition, according to the experimental data reported elsewhere,[34] the O_2/H_2O separation factor of silicone oil is 3.6.

Battery assembling and test

As-prepared LATP pellets, integration of thin LATP electrolyte and the carbon-coated LATP cathode with and without silicone-oil films, were transported into an Ar-filled glove box system (Etelux, Lab 2000) with oxygen and water contents below 1 ppm. The schematic diagram of the lithium-air battery is shown in Fig. S3. The galvanostatic charge and discharge tests were carried out on a battery test system (Neware, CT-3008 W) at different current densities (0.3 ~ 3 mA cm^{-2}) with a cutoff voltage of 2.0 V for the discharge process. The cycle performance was demonstrated with a fixed capacity of 1,000 and 5,000 mA h g^{-1}_{carbon} at a constant current density of 0.3 mA cm^{-2} in ambient air. To confirm the rate capability, the battery with a silicone-oil film was directly operated in ambient air at different current densities of 1, 2 and 3 mA cm^{-2}, respectively. All batteries were examined at room temperature in ambient air with a relatively high humidity of ~50%.

Characterization

The porosity, pore distribution and interior area of the novel porous cathode were investigated with mercury intrusion porosimetry (MIP, Micromeritics Instrument Corporation AutoPore IV 9500, USA). The morphologies for different kinds of cathodes at different depths of discharge were examined with scanning electron microscopy (SEM, JEOL-6700F and JEOL-6300) equipped with an energy dispersive spectrometer (EDS) that can be used as a microanalyzer, allowing accurate, efficient non-destructive element analysis or element distribution on the specimen. Transmission electron microscopy (TEM) images were obtained by operating a high-resolution JEOL 2010F TEM system with a LaB6 lament at 200 kV. The samples were dispersed in ethanol, sonicated and dripped onto the holey carbon-coated Cu grids. Attenuated total reflection Fourier transform infrared (ATR-FTIR, Vertex 70 Hyperion 1000) spectroscopy and X-ray photoelectron spectroscopy (XPS, Axis Ultra DLD, UK) were used to analyse the formation and decomposition of cathode products during discharge and charge processes. The contact angle was measured by a Digidrop Goniometer (GBX, DIGIDROP). The impedance spectra were recorded by an advanced electrochemical system (Parstat 2273, Princeton Instruments, USA) in the frequency range between 10^6 Hz and 0.1 Hz with a perturbation amplitude of 5 mV.

Results and discussion

Microscopy

As presented in Fig. 1a and b, the uppermost dense layer of the integrated LATP structure served as the electrolyte (19 μm thick and 96% dense), while the bottom porous layer (Fig. 1c) served as the cathode-support (75% porous). Since both the electrolyte layer and the cathode-support were prepared using the same material, LATP, the two layers were connected seamlessly *via* high-temperature sintering without the conventional interfacial resistance and potential barrier, thus resulting in a small Li^+ transport resistance between the electrolyte layer and the cathode. In this setup, the electrolyte layer does not exist independently but is a part of the entire system, lowering the demand for mechanical strength. Thus, the thickness can be reduced from several hundred micrometers to merely 19 μm to minimize ohmic loss. This novel cathode exhibits a high porosity of 75% and has the ability to create more pathways for gaseous oxygen molecules transporting directly to active sites with a much higher $P(O_2)$ and provide broader cavities for active material accommodation and solid product deposition. This is in contrast to conventional cathodes saturated with liquid electrolytes, whereby low oxygen solubility and transfer coefficient were commonly considered to be the rate-limiting steps for high-rate discharge processes.[41-43] Furthermore, the problem of evaporation in the open system lithium-air battery was eliminated due to the absence of liquid electrolytes at the cathode side. A carbon layer with a thickness of ~10 nm, as shown in Fig. 1d, was placed onto the interior surface of the LATP scaffold *via* an infiltration process to serve as both the electron conductor and the catalyst of the cathode. As a result, the active sites or TPBs were expanded from the conventional interface between the solid-state electrolyte and the cathode to the entire cathode with the help of LATP networks in providing three-dimensional Li^+ pathways through the cathode.

Discharge/charge performance and product characterization for the solid-state lithium-air battery without a silicone-oil film

The discharge and charge curves for the novel lithium-air battery without a silicone-oil film at a constant current density of 0.3 mA cm^{-2} are shown in Fig. 2a. In terms of discharge capacity, the battery delivered a value of 23,728 mA h g^{-1}_{carbon}. During the charge process, however, the battery was unable to undergo complete recharge, exhibiting merely 27% of the discharge capacity. A similar occurrence was reported by Zhou et al., in which a lithium-air battery exhibited a charge capacity of 3,400 mA h g^{-1}_{carbon} at 200 mA g^{-1}_{carbon} in air but only reached 18% of the discharge capacity.[12] XRD analysis showed that the discharge products mainly consisted of LiOH and Li_2O_2, and only LiOH was able to be recharged leaving isolative Li_2O_2. For this novel battery structure, however, XRD has been demonstrated to be inappropriate for the confirmation of discharge products, because the discharge product is formed and located inside the porous cathode and the LATP skeleton prevents X-rays from reaching the inner pores.[40] Therefore, further refined analysis of the cathodes was obtained by FTIR

and the results are illustrated in Fig. 3. Weak LiOH and/or Li_2CO_3 peaks were observed, but no significant Li_2O_2 peak (540 cm^{-1}) could be identified at the discharge terminal.[18] As widely reported,[42,43] Li_2O_2 is a typical product for the non-aqueous lithium-air battery under pure O_2 operation. In ambient air, the morphologies of the products inside the porous cathode after full discharge are noticeably different from the typical structure of Li_2O_2 (toroid or disc-like).[44,45] As presented in Fig. 2c, spinous particles were observed over the carbon surface after discharging to 3,000 mA h g^{-1}_{carbon} in ambient air. With an increase of the discharge depth, both the number of particles and the particle connections were observed to increase, as shown in Fig. 2d-e. For the following charge process, the number of particles decreased slightly in response to an increasing charge capacity. Even at the terminal stage, as shown in Fig. 2f, film-like products still remained on the carbon surface, which is consistent with the irreversible charge processes as shown in Fig. 2a. In this study, the spinous morphology for discharge products in ambient air should mainly derive from LiOH with a layer-like structure, as reported elsewhere.[46] For comparison, pure LiOH product, as shown in Fig. S4a, was obtained from a similar lithium-air battery that did not have a silicone-oil film after full discharge in pure O_2 at a relative humidity of 100% and a constant current density of 0.3 mA cm^{-2}. XPS spectrum in Fig. S4b confirms that the only product is LiOH. In this work, FTIR analysis was not used due to the location of LiOH overlapping with Li_2CO_3, as demonstrated by Fig. 3. The following equations show the speculated primary reactions at the cathode side in pure O_2 with the highest relative humidity of 100%:

$$2Li^+ + O_2 + 2e^- \rightarrow Li_2O_2 \quad (2)$$

$$2Li_2O_2 + 2H_2O \rightarrow 4LiOH + O_2 \quad (3)$$

As the primary product Li_2O_2 is highly reactive towards H_2O, it is understandable that the product at the terminal stage of the discharge process is LiOH alone, due to a lack of reactant CO_2. As illustrated in Fig. S4a, the product LiOH inside the porous cathode is loosely packed, which facilitates the transport of oxygen to active sites. As a result, the discharge process was greatly accelerated with a substantially improved discharge capacity of 81,984 mA h g^{-1}_{carbon}, which is more likely to provide an effective way to develop primary and/or aqueous lithium-air batteries. For conventional aqueous lithium-air batteries, the aqueous electrolytes readily permeate into the cathode pores to provide Li^+ transport pathways.[19,26,30,47] However, once a pore in the cathode is saturated with liquid electrolytes, the diffusion of gaseous oxygen is blocked, meaning that any subsequent electrochemical reactions will rely solely on the reaming dissolved oxygen in the electrolytes. If the batteries were to be operated in high relative humidity (RH), an ideal cathode can theoretically be achieved, in which all surface areas are fully wetted by a uniform thin water-film that can provide Li^+ transport pathways after dissolving LiO_x, while leaving more space for oxygen transport.

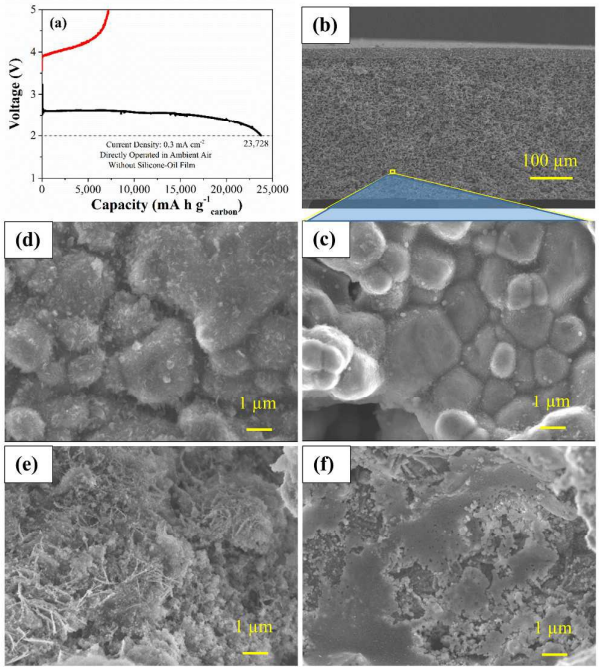

Fig. 2 (a) Typical galvanostatic charge/discharge curves of the proposed lithium-air batteries without a silicone-oil film operated in ambient air (~50% RH) at a constant current density of 0.3 mA cm^{-2}. Herein, the capacity densities were calculated by the mass of carbon loading (1.8 mg cm^{-2}). The SEM images for discharge products inside the battery cathode with a cutoff capacity of (b), (c) 3,000 mA h g^{-1}_{carbon}, (d) 10,000 mA h g^{-1}_{carbon} and (e) 23,728 mA h g^{-1}_{carbon}. (f) The SEM image for the cathode after recharging to 5.0 V.

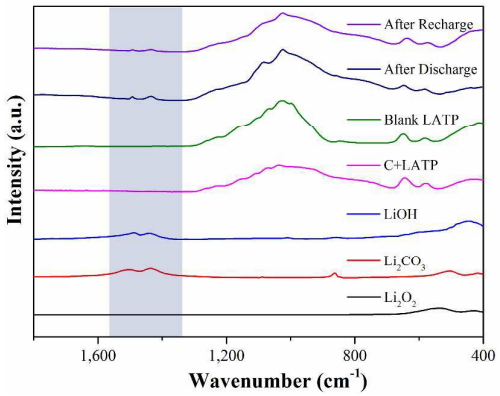

Fig. 3 Products formation and decomposition for the battery. FTIR spectra of a blank LATP cathode-support, only carbon-coated LATP cathodes, and the carbon-coated cathodes after the first discharge, then charge in ambient air. The discharge-charge behavior of the lithium-air battery is corresponding to Fig. 2a. The reference spectra for Li_2O_2, LiOH and Li_2CO_3 are also presented for comparison.

Discharge/charge performance and product characterization for the solid-state lithium-air battery with a silicone-oil film

Although rechargeable Li-CO_2 batteries have been reported, implying the ambient air operation of lithium-air battery is possible,[48,49] in this work, only 27% of the discharge capacity

was able to be recharged before charge voltage increased to 5.0 V. Silicone oil was thus chosen as the OSM to stabilize the operation of the battery in ambient air, which is used to select O_2 from ambient air to avoid the contamination of the revisable Li_2O_2. It has been reported that,[34,35] conventional OSMs are typically composed of a porous substrate and infiltrated silicone oil with a thickness of serval hundred micrometers and a limited interface area of several square centimeters between air and the OSMs. Even with this setup, these OSMs have an O_2/H_2O separation factor of 1.5-3.6 and a relatively high O_2 permeance of 2×10^{-7}-1.5×10^{-6} mol m^{-2} s^{-1} Pa^{-1} at room temperature.[34,35] Other kinds of OSMs usually involve an independent polymer membrane without a substrate, a thickness of >25 μm and an interface area of <20 cm^2 between air and the OSMs.[36,50] To summarize, the conventional OSMs with or without substrates were all placed near the exterior surface of the cathode as an independent layer, as shown in Fig. 4a. This setup has a large OSM thickness and a small interface between OSM and oxygen, and is suitable for a low-rate discharge battery due to a limited supply of O_2. This explains why lithium-air batteries with conventional OSMs usually operate at a low current density of 0.05 mA cm^{-2}.[34-36,50] In this work, a novel OSM was directly prepared into a porous cathode with the infiltration of silicone oil and intimately connected with cathode TPBs, as presented in Fig. 4b, achieving a minimized thickness (50 nm, about 0.01-1% of conventional planar OSMs) and a substantially expanded area for oxygen permeation (equal to the exposed area of the high porous cathode 330 cm^2 that is calculated based on the total pore area 0.7 m^2 g^{-1}_{LATP} as shown in Fig. S5). Fig. S5 depicts the median pore diameter (Volume) of the cathode at 7.3 μm, according to the MIP results. The median pore diameter (Area) is 1.1 μm that is consistent with Fig. 1c, and the average pore diameter ($4V/A$) is 2.9 μm. The porosity is demonstrated to be 75%, and the total pore area is confirmed to be 0.7 m^2 g^{-1}_{LATP}. Combining the mass of the cathode-support at 47 mg, we calculated the exposed area of the porous LATP cathode to be 330 cm^2, which is equal to the area of the silicone-oil film, over 10 times larger than that of conventional OSMs as shown in Fig. 4a. In this study, the thickness of the silicone-oil film was optimized by the following procedure. Silicone oil was first infiltrated into the carbon-coated LATP cathode, with different volumes, *i.e.*, 1 μL, 2 μL, 4 μL and 8 μL, and then dried in vacuum for 48 h before testing. The discharge curves of the four batteries were presented and compared in Fig. 5. The four batteries were all operated in ambient air (~50% RH) with a constant current density of 0.3 mA cm^{-2}. At the loading of 1 μL, the battery showed a maximum capacity of 17,000 mA h g^{-1}_{carbon}, 1.5 times of that for 2 μL one (11,000 mA h g^{-1}_{carbon}). However, the enhanced capacity should be attributed to the difference of product, rather than the reduced thickness of the silicone-oil film. As shown in Fig. 5 (right inset), the SEM image presents layer-like product in the leakage area, similar to that of the LiOH microstructure shown in Fig. S4a, indicating that the product for 1 μL silicone-oil infiltrated battery should be the mixture of LiOH and Li_2CO_3 but not revisable Li_2O_2 since the thin silicone-oil film was broken by product growth and agglomeration during the discharge process. Moreover, the discharge plateau of 2 μL silicone-oil infiltrated battery is slightly higher than that of the 1 μL one, suggesting the oxygen concentration at active sites is relatively high and further demonstrating the continuity and toughness of the 2 μL silicone-oil film. When increasing the volume to 4 μL or even 8 μL, the discharge plateau gradually disappears, as a result of an increase in the polarization for oxygen transporting through the thick silicone-oil films. As shown in Fig. 5 (left inset), at 8 μL the small pores that are bottlenecks were saturated with silicone oil, which severely blocks the transport of gaseous oxygen deep inside the cathode, resulting in serious polarization. Consistent with this observation, the polarization resistance of the battery was also increased with increasing volume, as demonstrated by impedance spectra at open circuit voltage (OCV) in ambient air (see Fig. S6). In the impedance spectra, the ohmic resistances saw very little change with an increase of volume. The ohmic resistance corresponding to the high-frequency intercept of the arc usually consists of electrolyte resistance, contact resistance and electrode ohmic resistance.[51,52] For the solid-state lithium-air battery, the resistance of Li^+ through the solid-state electrolyte is a major component of ohmic resistance because of the limited conductivity. According to the thickness of the LATP electrolyte layer (19 μm in Fig. 1b) and the ohmic resistance (14 Ω cm^2 in Fig. S6), we calculated the conductivity of the LATP electrolyte layer to be 1.3×10^{-4} S cm^{-1}, which is consistent with previous reports.[10,12,13,53]

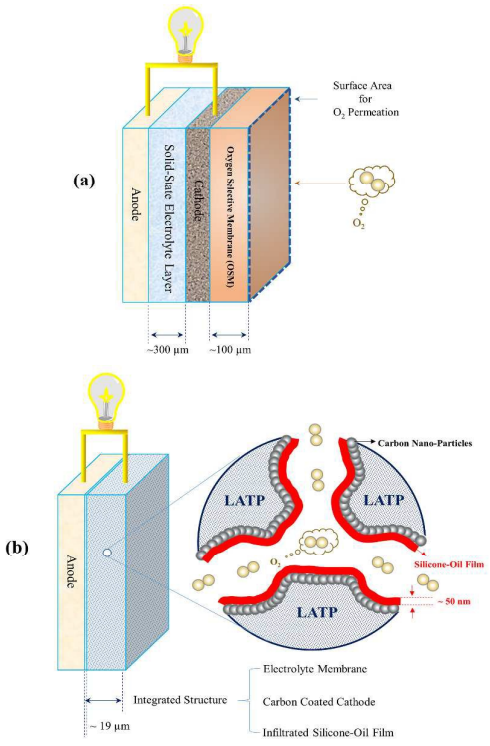

Fig. 4 Schematic representations of architectures for (a) conventional solid-state lithium-air batteries with a thick solid-state electrolyte layer and a planar oxygen selective membrane (planar OSM) external to

cathode, and (b) the proposed solid-state lithium-air batteries with an integrated structure of solid-state LATP membrane, carbon-coated LATP cathode and a silicone-oil film inside the cathode.

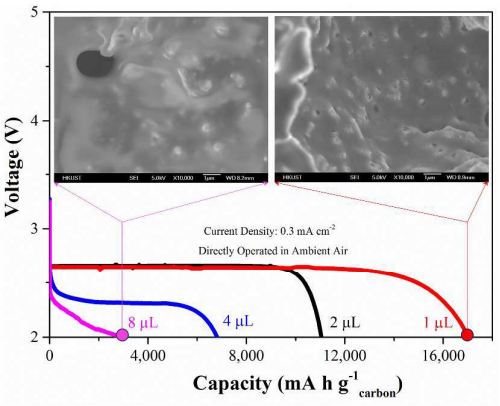

Fig. 5 Typical galvanostatic discharge curves for the proposed lithium-air batteries with silicone-oil films, operated in ambient air (~50% RH) at a constant current density of 0.3 mA cm^{-2}. The silicone-oil films with different thicknesses were prepared by an infiltrating process with different volumes of silicone oil, *i.e.*, 1 μL, 2 μL, 4 μL and 8 μL after drying in vacuum for 48 h. The SEM image (right inset) is used to display the microstructure and distribution of discharge products and the crack of the 1 μL silicone-oil deposited film after full discharge to 2.0 V, while the SEM image (left inset) is used to display the channel plugging in the 8 μL silicone-oil infiltrated cathode after full discharge to 2.0 V.

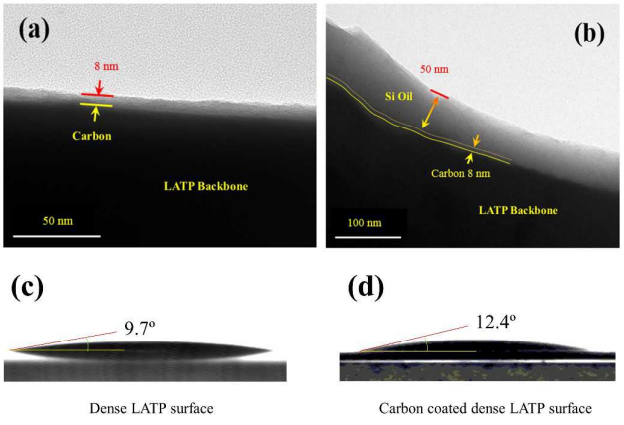

Fig. 6 High-resolution view of the outer portion of LATP grain and surface layer. The TEM imgage (a) is for only carbon-coated LATP cathode, while (b) is for carbon and then 2 μL silicone-oil infiltrated cathode prior to operation. The contact angles of silicone-oil on (c) the dense LATP surface and (d) the carbon-coated dense LATP surface.

2 μL as an optimized volume will be adopted in the following experiments. Fig. S7 shows EDS results of the porous LATP cathode with the silicone-oil film, demonstrating the uniform distribution of silicone oil over the carbon-coated LATP surface. As shown in Fig. 6, it can be seen from the view of an LATP particle taken from (a) only the carbon-coated cathode and (b) the carbon and then 2 μL silicone-oil infiltrated cathode that it is coated with a uniform and continuous surface film whose projected thickness is 8 nm and 50 nm for the carbon layer and silicone-oil film, respectively. The small contact angles shown in Fig. 6c and d suggest that silicon oil can wet the pore surfaces of cathode and exists in the form of films, although the thickness of the silicone-oil film might undergo a slight change at the LATP grain boundary. As the silicone-oil film is rather thin, about 50 nm, the surface tension determines the profile of the film on the surface of LATP support. As a result, the film distribution follows the surface profile, as shown in Fig. 6b. It is apparent for the interface between LATP and carbon but not for the interface between carbon and silicone oil since the two amorphous structures have similar light transmittances. We can calculate the average thickness of silicone oil over the carbon surface by using the volume of silicone oil 2 μL and the interior pore area of 330 cm^2, to be at around 60 nm, close to the experimental result of ~50 nm as illustrated in Fig. 6b.

Table 1 The comparison of configuration, performance and operating condition between the conventional lithium-air batteries with planar OSMs external to cathodes and the proposed lithium-air batteries with the silicone-oil films inside cathodes.

OSM	Interface of OSM/O_2 (cm^2)	OSM thick (μm)	Relative humidity (%)	Current density (mA cm^{-2})	Specific capacity (mA h g^{-1}_{carbon})
Silicone oil + porous metal	1.98	50	30	0.05	240[34]
Silicone oil + PDMS treated porous metal	1.98	50	30	0.05	280[34]
Commercial PTFE	1.98	102	30	0.05	160[34]
Commercial PTFE	1.98	102	<1	0.05	170[34]
Silicone oil + Silicalite/porous metal	1.98	50	20	0.05	770[34]
Silicone oil + PFE	1.98	102	20	0.05	789[34]
Commercial PTFE	1.98	102	20	0.05	267[34]
Commercial PTFE	1.98	102	<1	0.05	630[34]
Plastic membrane	16.8	25	~20	0.05	2,711[50]
Plastic membrane	16.8	25	~20	0.1	1,807[50]
Polysiloxane methacrylate (Primary battery)	10	330	15	0.1	947[37]
Polysiloxane methacrylate (Primary battery)	10	432	15	0.1	818[37]
Polysiloxane methacrylate (Primary battery)	10	83	42.9	0.2	570[37]
Teflon coated fiberglass cloth (Primary battery)	10	--	20	0.1	2,000~6,000[37] With different liquid electrolytes

Silicone-oil film in this work	330	0.05	~50	0.3	11,697
Silicone-oil film in this work	330	0.05	~50	1	6,902
Silicone-oil film in this work	300	0.05	~50	2	2,849

In addition to blocking the penetration of moisture from ambient air into the lithium-air batteries, the OSM may also prevent loss of the electrolyte solvent due to evaporation. In this novel cathode configuration, however, liquid electrolyte was absent, so that the silicone-oil film is of no particular use in this respect. But precisely because of the absence of liquid electrolyte, directly placing a silicone-oil film into the porous cathode is possible. Moreover, in this novel cathode, the silicone-oil film was connected with the active substance as closely as possible, which further shortens the transport route of oxygen from ambient air to TPBs. In contrast, for lithium-air batteries with conventional planar OSMs, as shown in Fig. 4a, permeated oxygen species from OSMs must be dissolved into liquid electrolytes first, and then diffused from one interface between the electrolyte and OSM to another interface between the electrolyte and cathode (active sites) with liquid electrolytes as the media. As a result, the oxygen flux is determined by three processes: (i) the oxygen permeation through OSMs, (ii) the oxygen dissolution into liquid electrolytes, and (iii) the oxygen diffusion inside liquid electrolytes. For the proposed cathode, the oxygen flux is mainly determined by the oxygen permeation through silicone-oil films, whose area was expanded to over 10 times in size and whose thickness was decreased to nearly one in a thousand *via* the infiltration technique.

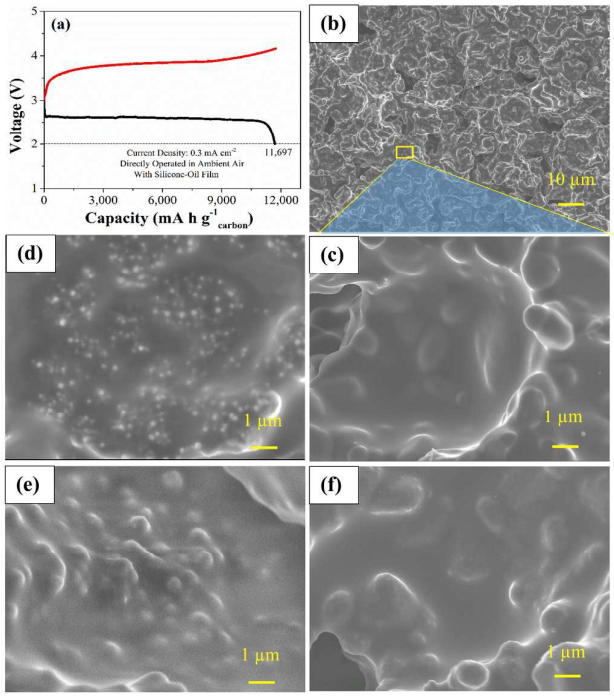

Fig. 7 (a) Typical galvanostatic charge/discharge curves of the proposed lithium-air batteries with a silicone-oil film operated in ambient air (~50% RH) at a constant current density of 0.3 mA cm^{-2}. Herein, the capacity densities were calculated by the mass of carbon loading (1.8 mg cm^{-2}). The SEM images for discharge products inside the cathode of battery with a cutoff capacity of (b), (c) 0 mA h g^{-1}_{carbon} (d) 5,000 mA h g^{-1}_{carbon} and (e) 11,697 mA h g^{-1}_{carbon}. (f) The SEM image for the cathode after the recharging process.

As shown in Fig. 7a, a lithium-air battery based on the novel integrated LATP structure coated with the silicone-oil film exhibited a discharge capacity of 11,697 mA h g^{-1}_{carbon} and a voltage plateau of 2.62 V (*vs* Li^+/Li) in ambient air. This specific capacity is several times higher than that of the lithium-air battery based on liquid electrolytes with conventional OSM structures, as listed in Table 1. To the best of our knowledge, many previous works focused on the discharge process rather than the recharge process. In this work, the recharge process is presented in Fig. 7a. Only one voltage plateau of about 3.8 V was observed in the recharge curve, and the terminal voltage was 4.3 V, indicating that it is possible to fully recharge the battery. The voltage plateau is obviously lower than that of a similar battery without the silicone-oil film (merely 27% recharged, Fig. 2a), and even lower than that of various liquid electrolyte-based lithium-air batteries, especially at the terminal stage, suggesting an improved energy efficiency.[3,24,33]

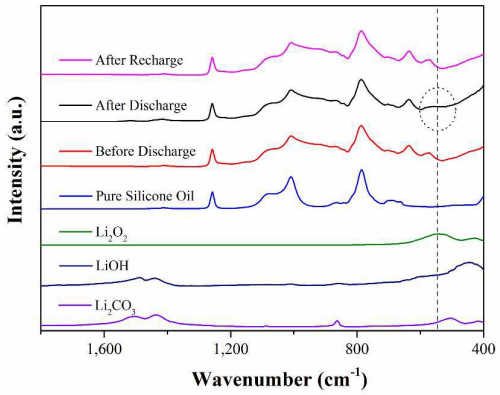

Fig. 8 Products formation and decomposition in ambient air for the proposed lithium-air battery with a silicone-oil film. FTIR spectra of pure silicone oil, silicone oil and carbon-coated LATP cathode (marked as before discharge process), and the cathodes after the first discharge, then charge in ambient air. The discharge/charge behavior of the lithium-air battery is corresponding to Fig. 7. The reference spectra for Li_2O_2, LiOH and Li_2CO_3 are also presented for comparison.

Fig. 7b-e show the comparison of the SEM images for the battery cathodes at different depths of the discharge process. As displayed in Fig. 7b and c, a pristine cathode with two uniform thin layers (up silicone-oil film 50 nm thick and down carbon layer 8 nm thick) are placed onto the LATP scaffold. At a discharge capacity of 5,000 mA h g^{-1}_{carbon} (Fig. 7d), the coating surface becomes uneven, suggesting that small particles generate under the silicone-oil film. At the terminal stage of the discharge process (Fig. 7e), the particle size was found to increase, which may be caused by an agglomeration of small

particles. Unlike in Fig. 5 (right inset), the agglomeration was not to be blamed for cracking or breaking of the silicone-oil film even at the terminal stage, demonstrating the robust thickness of the 2 μL film. Furthermore, the introduction of the silicone-oil film restricts the discharge products to a limited space that is fairly close to the active sites, which facilitates the recharge process. After a full recharge (Fig. 7f), the film surface becomes even again, suggesting product decomposition, which is consistent with the reversible discharge and charge curves in Fig. 7a. Further evidence has been obtained from FTIR analysis, as illustrated in Fig. 8, where the formation and decomposition of Li_2O_2 are clearly identified in the FTIR spectra. The weak peak for Li_2O_2 can be attributed to the following two reasons: i) in the FTIR spectra, the peak of Li_2O_2 overlaps the valley of LATP near 540 cm^{-1}; and ii) during the FITR test, the product Li_2O_2 was covered by a silicone-oil film.

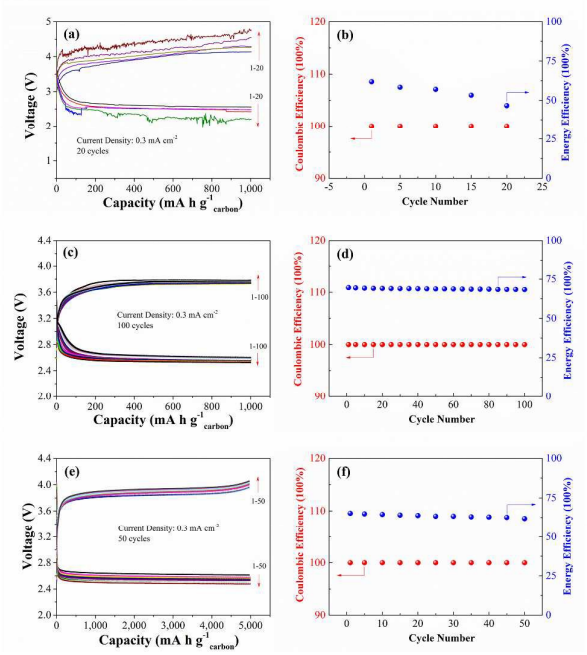

Fig. 9 (a), (b) Cycling performance of the proposed lithium-air battery without a silicone-oil film in ambient air under a capacity limitation of 1,000 mA h g^{-1}_{carbon} for 20 cycles; (c), (d) cycling performance of the proposed lithium-air battery with a silicone-oil film in ambient air under a capacity limitation of 1,000 mA h g^{-1}_{carbon} for 100 cycles; and (e), (f) cycling performance of the proposed lithium-air battery with a silicone-oil film in ambient air under a capacity limitation of 5,000 mA h g^{-1}_{carbon} for 50 cycles.

Cycle performances and high-rate discharge properties for the solid-state lithium-air battery with a silicone-oil film

To evaluate and compare the cycle performance, the proposed lithium-air battery without the silicone-oil film was cycled directly in ambient air (~50% RH) with a fixed capacity of 1,000 mA h g^{-1}_{carbon} at a constant current density of 0.3 mA cm^{-2}. Discharge/charge curves of the battery at cycles of 1, 5, 10, 15 and 20 are illustrated in Fig. 9a. Oscillation phenomenon in discharge/charge potentials became apparent at cycle 15, which is associated with the formation and decomposition of Li_2CO_3 on cycling, as suggested in previous reports.[12] After only 20 cycles, the energy efficiency decreased from 62% to 47%, as shown in Fig. 9b, with a voltage plateau of discharge decreasing from 2.56 V to about 2.21 V and the charge plateau increasing from 4.13 V to 4.74 V.

Fig. 9c shows the different discharge/charge curves for the lithium-air battery with the silicone-oil film and a fixed capacity of 1,000 mA h g^{-1}_{carbon} at a constant current density of 0.3 mA cm^{-2} in ambient air. The capacity retention on cycling is shown in Fig. 9d, from which 100% of the initial capacity is retained after 100 cycles. Moreover, the energy efficiency during cycling decreased slightly from 69% to 67%, with the voltage plateau of discharge decreasing from 2.61 to 2.53 V while the voltage plateau of charge increasing from 3.77 to 3.78 V. Cycle performance of the battery at a fixed capacity of 5,000 mA h g^{-1}_{carbon} was further tested. After 50 cycles, the energy efficiency during cycling decreased from 65% to 61%, as shown in Fig. 9f. Therefore, the battery with a silicone-oil film was demonstrated to have a substantially enhanced cycling stability.

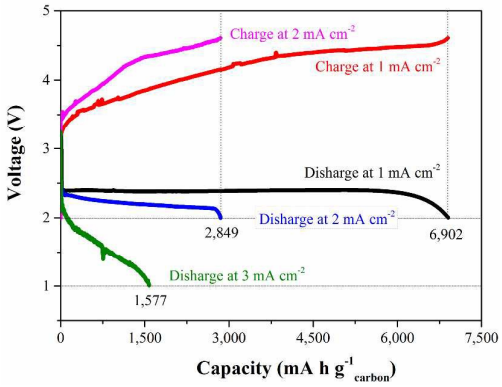

Fig. 10 Galvanostatic discharge/charge curves (*U* vs capacity) for the proposed lithium-air battery with a silicone-oil film operated in ambient air at a current density of 1, 2 and 3 mA cm^{-2}.

In this study, minimizing the thicknesses of the solid-state electrolyte layer and OSM and expanding the interfaces of the cathode/electrolyte and of the OSM/oxygen is aimed at bringing an improvement of both the mass transport and TPBs, which is intimately intertwined with the rate capability of the battery and thus prompts us to investigate the rate performance of the novel lithium-air battery. Fig. 10 shows that the lithium-air battery maintained a continuous discharge voltage plateau with increasing current densities. A discharge capacity of 2,849 mA h g^{-1}_{carbon} was still obtained at a high current density of 2 mA cm^{-2}. For comparison, we also fabricated a LATP electrolyte and a porous LATP cathode separately, and connected the two components. However, this two-component-connected battery did not work because of the poor contact between the electrolyte layer and the cathode. To reduce the contact resistance, a LATP paste (70 wt% LATP powder + 30 wt% terpilenol) was filled at the interface and was sintered at

800 ºC for 3 h. As shown in Fig. S8, the battery exhibited a peak current density of 0.005 mA cm^{-2}, which is only 1% of that of the lithium-air battery with the integrated electrolyte and cathode. Much of the literature to date focuses on investigating conventional lithium-air batteries with planar OSMs limited to current densities of around 0.05 mA cm^{-2}.[34-37] In this work, the integrated lithium-air battery has been demonstrated to be directly operated in ambient air (~50% RH), with a substantially enhanced specific capacity and excellent cycle performance, which reveals a new avenue for the improvement of the three-phase reaction for an air cathode. This will result in the study of an integrated structure and the novel OSM for research on practical lithium-air batteries.

Conclusions

This work demonstrates that the designed novel lithium-air battery can be operated in ambient air reversibly with high performance. The integrated solid-state electrolyte and cathode structure after carbon coating allows the superior 3D tri-continuous passage of electrons, ions, and oxygen, which is able to extend the triple-phase boundary to the entire cathode. At the cathode side, there are no liquid electrolytes, thus fundamentally addressing the inherent evaporation problem for open system lithium-air batteries. As such, an oxygen selective membrane (OSM) was allowed to be directly prepared onto the porous solid-state cathode and connected with active sites as closely as possible, resulting in an expanded interface between OSM and O_2 (330 cm^2) and a minimized thickness (50 nm). Consequently, the integrated lithium-air battery with a silicone-oil film as the OSM exhibited a prominent specific capacity of 11,697 mA h g^{-1}_{carbon} with a discharge voltage plateau of 2.62 V (*vs* Li^+/Li), when operated in ambient air (~50% relative humidity) at a constant current density of 0.3 mA cm^{-2}. More importantly, it can be completely recharged with a relatively low charge potential plateau of 3.8 V. In contrast, a similar lithium-air battery without a silicone-oil film exhibited a much higher specific energy density of 23,728 mA h g^{-1}_{carbon} under the same testing conditions, but could only be recharged to 27% of the discharge capacity. To demonstrate stability, the novel solid-state battery installed with a silicone-oil film can sustain repeated cycling for 100 and 50 cycles at a fixed capacity of 1,000 mA h g^{-1}_{carbon} and 5,000 mA h g^{-1}_{carbon} in ambient air, respectively, with a stable coulombic efficiency (100%) and no more than 5% decrease in energy efficiency. Furthermore, the discharge current density for the novel battery was increased to 2 mA cm^{-2}, a value much higher than that of conventional OSM protected lithium-air batteries (0.05 mA cm^{-2}). As demonstrated above, this battery design solves two major problems, namely high ohmic loss and limited active interface in solid-state lithium-air batteries, and accomplishes the air operation of the lithium-air battery *via* the introduction of a novel silicone-oil film as OSM, showing the potential applications as a power source in electric vehicles.

Acknowledgements

The work described in this paper was fully supported by a grant from the Research Grants Council of the Hong Kong Special Administrative Region, China (Project No. 16213414).

Notes and references

1. H. G. Jung, J. Hassoun, J. B. Park, Y. K. Sun and B. Scrosati, *Nat. Chem.*, 2012, **4**, 579-585.
2. G. Girishkumar, B. D. McCloskey, A. C. Luntz, S. Swanson and W. Wilcke, *J. Phys. Chem. Lett.*, 2010, **1**, 2193-2203.
3. A. C. Luntz and B. D. McCloskey, *Chem. Rev.*, 2014, **114**, 11721-11750.
4. F. T. Wagner, B. Lakshmanan and M. F. Mathias, *J. Phys. Chem. Lett.*, 2010, **1**, 2204-2219.
5. Z. L. Wang, D. Xu, J. J. Xu and X. B. Zhang, *Chem. Soc. Rev.*, 2014, **43**, 7746-7786.
6. J. J. Xu, Z. L. Wang, D. Xu, F. Z. Meng and X. B. Zhang, *Energy Environ. Sci.*, 2014, **7**, 2213-2219.
7. J. Wang, Y. Li and X. Sun, *Nano Energy*, 2013, **2**, 443-467.
8. Y. Shao, S. Park, J. Xiao, J. G. Zhang, Y. Wang and J. Liu, *Acs Catal.*, 2012, **2**, 844-857.
9. R. Black, B. Adams and L. Nazar, *Adv. Energy Mater.*, 2012, **2**, 801-815.
10. Y. Sun, *Nano Energy*, 2013, **2**, 801-816.
11. Q. C. Liu, J. J. Xu, D. Xu and X. B. Zhang, *Nat. Commun.*, 2015.
12. T. Zhang and H. S. Zhou, *Nat. Commun.*, 2013, **4**, 1811-1817.
13. X. Wang, D. Zhu, M. Song, S. Cai, L. Zhang and Y. Chen, *ACS Appl. Mater. Inter.*, 2014, **6**, 11204-11210.
14. N. Akhtar and W. Akhtar, *Int. J. Energy Res.*, 2015, **39**, 303-316.
15. L. Grande, E. Paillard, J. Hassoun, J. Park, Y. Lee, Y. Sun, S. Passerini and B. Scrosati, *Adv. Mater.*, 2015, **27**, 784-800.
16. C. O. Laoire, S. Mukerjee, K. Abraham, E. J. Plichta and M. A. Hendrickson, *J. Phys. Chem. C*, 2011, **114**, 9178-9186.
17. B. Scrosati and J. Garche, *J. Power Sources*, 2010, **195**, 2419-2430.
18. Z. Peng, S. A. Freunberger, Y. Chen and P. G. Bruce, *Science*, 2012, **337**, 563-566.
19. B. McCloskey, D. Bethune, R. Shelby, G. Girishkumar and A. Luntz, *J. Phys. Chem. Lett.*, 2011, **2**, 1161-1166.
20. J. J. Xu, D. Xu, Z. L. Wang, H. G. Wang, L. L. Zhang and X. B. Zhang, *Angew. Chem. Int. Ed.*, 2013, **52**, 3887-3890.
21. B. Kumar, J. Kumar, R. Leese, J. P. Fellner, S. J. Rodrigues and K. Abraham, *J. Electrochem. Soc.*, 2010, **157**, A50-A54.
22. E. Quartarone and P. Mustarelli, *Chem. Soc. Rev.*, 2011, **40**, 2525-2540.
23. T. Zhang, N. Imanishi, Y. Shimonishi, A. Hirano, Y. Takeda, O. Yamamoto and N. Sammes, *Chem. Commun.*, 2010, **46**, 1661-1663.
24. M. A. Rahman, X. Wang and C. Wen, *J. Appl. Electrochem.*, 2014, **44**, 5-22.
25. F. Li, T. Zhang and H. S. Zhou, *Energy Environ. Sci.*, 2013, **6**, 1125-1141.
26. N. Garcia-Araez and P. Novák, *J. Solid State Electr.*, 2013, **17**, 1793-1807.
27. J. J. Xu, Z. L. Wang, D. Xu, L. L. Zhang and X. B. Zhang, *Nat. Commun.*, 2013, **4**, 1811-1817.
28. H. K. Lim, H. D. Lim, K. Y. Park, D. H. Seo, H. Gwon, J. Hong, W. A. Goddard III, H. Kim and K. Kang, *J. Am. Chem. Soc.*, 2013, **135**, 9733-9742.
29. Z. Guo, X. Dong, S. Yuan, Y. Wang and Y. Xia, *J. Power Sources*, 2014, **264**, 1-7.
30. B. D. Adams, R. Black, Z. Williams, R. Fernandes, M. Cuisinier, E. J. Berg, P. Novak, G. K. Murphy and L. F. Nazar, *Adv. Energy Mater.*, 2015, **5**.

31. M. D. Bhatt, H. Geaney, M. Nolan and C. O'Dwyer, *Phys. Chem. Chem. Phys.*, 2014, **16**, 12093-12130.
32. O. Crowther and M. Salomon, *Membranes*, 2012, **2**, 216-227.
33. Y. Shao, F. Ding, J. Xiao, J. Zhang, W. Xu, S. Park, J. G. Zhang, Y. Wang and J. Liu, *Adv. Funct. Mater.*, 2013, **23**, 987-1004.
34. J. Zhang, W. Xu and W. Liu, *J. Power Sources*, 2010, **195**, 7438-7444.
35. J. Zhang, W. Xu, X. Li and W. Liu, *J. Electrochem. Soc.*, 2010, **157**, A940-A946.
36. J. G. Zhang, D. Wang, W. Xu, J. Xiao and R. E. Williford, *J. Power Sources*, 2010, **195**, 4332-4337.
37. O. Crowther, B. Meyer, M. Morgan and M. Salomon, *J. Power Sources*, 2011, **196**, 1498-1502.
38. J. Christensen, P. Albertus, R. S. Sanchez-Carrera, T. Lohmann, B. Kozinsky, R. Liedtke, J. Ahmed and A. Kojic, *J. Electrochem. Soc.*, 2011, **159**, R1-R30.
39. E. C. Bucharsky, K. G. Schell, A. Hintennach and M. J. Hoffmann, *Solid State Ionics*, 2015, **274**, 77-82.
40. X. B. Zhu, T. S. Zhao, Z. H. Wei, P. Tan and G. Zhao, *Energy Environ. Sci.*, 2015, **8**, 2782-2790.
41. R. Padbury and X. Zhang, *J. Power Sources*, 2011, **196**, 4436-4444.
42. S. Sandhu, J. Fellner and G. Brutchen, *J. Power Sources*, 2007, **164**, 365-371.
43. J. Suntivich, H. A. Gasteiger, N. Yabuuchi, H. Nakanishi, J. B. Goodenough and Y. Shao-Horn, *Nat. Chem.*, 2011, **3**, 546-550.
44. Y. C. Lu, B. M. Gallant, D. G. Kwabi, J. R. Harding, R. R. Mitchell, M. S. Whittingham and Y. Shao-Horn, *Energy Environ. Sci.*, 2013, **6**, 750-768.
45. F. Marchini, S. Herrera, W. Torres, A. Y. Tesio, F. J. Williams and E. J. Calvo, *Langmuir*, 2015, **31**, 9236-9245.
46. G. Hasegawa, K. Kanamori, Y. Sugawara, Y. Ikuhara and K. Nakanishi, *J. Colloid Interf. Sci.*, 2012, **374**, 291-296.
47. Y. C. Lu, H. A. Gasteiger and Y. Shao-Horn, *J. Am. Chem. Soc.*, 2011, **133**, 19048-19051.
48. Y. Liu, R. Wang, Y. Lyu, H. Li and L. Chen, *Energy Environ. Sci.*, 2014, **7**, 677-681.
49. Z. Zhang, Q. Zhang, Y. Chen, J. Bao, X. Zhou, Z. Xie, J. Wei and Z. Zhou, *Angew. Chem. Int. Ed.*, 2015, **54**, 6550-6553.
50. D. Wang, J. Xiao, W. Xu and J. G. Zhang, *J. Electrochem. Soc.*, 2010, **157**, A760-A764.
51. J. Højberg, B. D. McCloskey, J. Hjelm, T. Vegge, K. Johansen, P. Norby and A. C. Luntz, *ACS Appl. Mater. Inter.*, 2015, **7**, 4039-4047.
52. I. Bardenhagen, O. Yezerska, M. Augustin, D. Fenske, A. Wittstock and M. Bäumer, *J. Power Sources*, 2015, **278**, 255-264.
53. B. Key, D. J. Schroeder, B. J. Ingram and J. T. Vaughey, *Chem. Mater.*, 2012, **24**, 287-293.